Received: 21 March 2016 | Revised: 5 July 2016 | Accepted: 12 August 2016

DOI 10.1002/cnm.2824

WILEY

RESEARCH ARTICLE

Data assimilation for identification of cardiovascular network characteristics

Rajnesh Lal* | **Bijan Mohammadi** | **Franck Nicoud**

IMAG, Universite de Montpellier, Montpellier, CC051, 34095, France

Correspondence
Rajnesh Lal, IMAG, Universite de Montpellier, CC051, 34095 Montpellier, France.
Email: rajnesh.lal@etu.umontpellier.fr

Abstract

A method to estimate the hemodynamics parameters of a network of vessels using an Ensemble Kalman filter is presented. The elastic moduli (Young's modulus) of blood vessels and the terminal boundary parameters are estimated as the solution of an inverse problem. Two synthetic test cases and a configuration where experimental data are available are presented. The sensitivity analysis confirms that the proposed method is quite robust even with a few numbers of observations. The simulations with the estimated parameters recovers target pressure or flow rate waveforms at given specific locations, improving the state-of-the-art predictions available in the literature. This shows the effectiveness and efficiency of both the parameter estimation algorithm and the blood flow model.

KEYWORDS

1D blood flow, ensemble Kalman filter, inverse problem, parameter estimation

1 | INTRODUCTION

An increase in arterial stiffness has been shown to be linked with age including other health problems or risk factors such as diabetes and hypertension.[1] The stiffness of arteries can be measured using different techniques such as by measuring the pulse wave velocity (PWV) or with the analysis of local variations in local pressure and volume.[2] Pulse wave velocity is directly related to the arterial wall elasticity and to the Young's modulus of the arteries.[2]

"Assimilation is the process of finding the model representation which is most consistent with the observations".[3] The use of inaccurate parameters in the model equations can give rise to model errors.[4] The parameter estimation problem tends to improve initial estimates of the model parameters so that the difference between the measurements and the model solution are minimized. In parameter estimation problem, it is assumed that the uncertainties in the model parameters are the sources of errors for the model errors.[5] According to Annan et al.,[6] it is important to tune the parameters to gain a better confidence in the predictions of the state values. Generally, we have observable data for the state, but no direct observable data for the parameters.

In recent years, parameter estimation has been carried out using a similar framework as for the state estimation. The state vectors can be augmented by the poorly known parameters for estimating by having a Kalman filter for the state-parameter augmented model.[5,7–9] In state-parameter augmentation, parameters are considered as part of the model, which are updated in the analysis step of the data assimilation algorithm together with the model variables.[6] An evolution model for model parameters is required for the state-parameter augmented model.[10] The common evolution model includes the random walk model[11,12] and the persistence model.[9,13] Combining the model variables and model parameters during the analysis step can also introduce problems such as parameter collapse and filter divergence.[14] In studies elsewhere,[14,15] parameter estimation using an ensemble Kalman filter (EnKF) is presented using augmentation method, but without updating the model states during the assimilation step.

Some recent works on inverse problems in hemodynamics include the work of Lombardi,[16] Moireau et al.,[17] Pant et al.,[18] Bertoglio et al.,[19] Chabiniok et al.,[20] Martin et al.,[21] Spilker et al.,[22] and Lassila et al.[23] In Lombardi,[16] a sequential approach based on the reduced-order unscented

Kalman filter (ROUKF) is presented for the identification of arterial stiffness parameters in 1D hemodynamics. In Moireau et al.,[17] ROUKF is used to identify the boundary condition parameters in a fluid structure vascular model utilizing patient image data. In Pant et al.,[18] a sequential estimation technique using the unscented Kalman filter (UKF) is presented to estimate lumped model parameters from clinical measurements. In Bertoglio et al.,[19] parameter estimation using ROUKF for fluid-structure interaction problems is presented. In Chabiniok et al.,[20] the use of sequential joint state-parameter data assimilation to a biomechanical heart model with actual cardiac Cine-MRI data is presented. In Martin et al.,[21] a variational method (adjoint state approach) is presented to identify the parameters of 1D models for blood flow in arteries. In Spilker et al.,[22] a quasi-Newton method is used to adjust the parameters of the outlet boundary conditions of blood flow models to achieve target profiles of flow and pressure waveforms. In Lassila et al.,[23] the solution of inverse problems in hemodynamics is proposed using deterministic and Bayesian approaches.

Recent works on inverse problems in hemodynamics are either based on joint state augmented model (e.g., Chabiniok et al.[20]) or ROUKF (eg, Lombardi,[16] Moireau et al.,[17] Pant et al.,[18] and Bertoglio et al.[18]). We use EnKF to identify the Young's modulus and the terminal boundary parameters as the solution of inverse problems. Our aim is to show that this can be achieved with only a few number of observations and without using the joint state formulation, hence reducing a modification of the state equations. We think this is important in order to minimize the coupling between the assimilation tool and the state equations solver. Also, one originality is to ensure positivity for the solutions of the inversion introducing an adequate reformulation of the problem through logarithmic variable changes. Finally, one important result of the paper is to show that joint use of data assimilation and flow solution by a CFD code greatly improves available results in the literature for a realistic human arterial model with available experimental references.[24]

In this paper, first we present a review of the data assimilation method using an EnKF and propose a method for hemodynamics parameter estimation as the solution to an inverse problem. In the second section a blood flow model of the cardiovascular network is presented. In Section 3, test cases are presented where we show the applicability of an EnKF to 1D blood flow model in parameter estimation. The first two test cases use synthetic data and the final test case involves the use of an experiments data.[24] The test cases are limited to the estimation of Young's modulus and the boundary condition parameter, i.e., reflection coefficient and the viscoelastic coefficient.

2 | ENSEMBLE KALMAN FILTER

First introduced by Geir Evenson,[25] an EnKF solves the Fokker-Plank equation using a Monte Carlo or ensemble integrations.[26] It is a suboptimal estimator for problems involving high-order nonlinear models. The error statistics are predicted using the ensemble of states. Different versions of EnKF are available in the literature: Deterministic Ensemble Kalman filter,[27] Monte Carlo EnKF,[25,28] EnKF,[29,30] Hybrid EnKF,[31] Ensemble Transform Kalman filter,[32] Ensemble Adjustment Kalman filter,[7] Ensemble Square Root filters,[33] and Local Ensemble Kalman filter.[34]

2.1 | Derivation of ensemble Kalman filter

In EnKF the forecast error covariance matrix is evaluated using an ensemble of forecasts. In this section we follow and describe the different steps employed in the formulation of EnKF as presented elsewhere.[30,35–38]

We will assume that the discrete nonlinear system is described by

$$\mathbf{x}_{k+1} = f(\mathbf{x}_k) + \mathbf{w_k}, \quad \mathbf{y}_k = h(\mathbf{x}_k) + \mathbf{v_k}. \tag{1}$$

The model state at time t_k is $\mathbf{x}_k \in \mathbb{R}^n$, while the observed state is $\mathbf{y}_k \in \mathbb{R}^p$. n is the dimension of the model state vector and p is the number of observations. $\mathbf{w}_k \in \mathbb{R}^n$ and $\mathbf{v}_k \in \mathbb{R}^p$ are assumed uncorrelated Gaussian model errors with $\mathbf{w}_k \sim \mathcal{N}(0, \mathbf{Q_k})$ and $\mathbf{v}_k \sim \mathcal{N}(0, \mathbf{R_k})$, where $\mathbf{Q_k}$ and $\mathbf{R_k}$ are the covariance matrices. h is the function describing the relationship between the measurement and the states.

At time t_k it is assumed that an ensemble of q forecast state estimates (prior ensembles); $\mathbf{X}_k^{\mathrm{f}} = (\mathbf{x}_k^{\mathrm{f}_1}, \dots, \mathbf{x}_k^{\mathrm{f}_q}) \in \mathbb{R}^{n\times q}$ is available. f_i represents the ith forecast member of the ensemble. The mean of the ensemble of forecast state is $\bar{\mathbf{x}}_k^{\mathrm{f}} \in \mathbb{R}^n$ and is given by

$$\bar{\mathbf{x}}_k^{\mathrm{f}} = \frac{1}{q}\sum_{i=1}^{q} \mathbf{x}_k^{\mathrm{f}_i}. \tag{2}$$

The forecast covariance matrix, $\mathbf{P}_k^{\mathrm{f}} \in \mathbb{R}^{n\times n}$, is defined by

$$\mathbf{P}_k^{\mathrm{f}} = \frac{1}{q-1}\sum_{i=1}^{q}\left(\mathbf{x}_k^{\mathrm{f}_i} - \bar{\mathbf{x}}_k^{\mathrm{f}}\right)\left(\mathbf{x}_k^{\mathrm{f}_i} - \bar{\mathbf{x}}_k^{\mathrm{f}}\right)^{\mathrm{T}}. \tag{3}$$

After the computation of the Kalman gain $\mathbf{K}_k$, all operations on the ensemble members are independent in the EnKF analysis step and the ensemble members are updated using

$$\mathbf{x}_k^{\mathrm{a}_i} = \mathbf{x}_k^{\mathrm{f}_i} + \mathbf{K}_k\left[\mathbf{y}_k^i - h\left(\mathbf{x}_k^{\mathrm{f}_i}\right)\right], \quad i = 1, \dots, q, \tag{4}$$

where a_i represents the ith updated or analysed member of the ensemble. Without adding perturbations to the original observation vector, an updated ensemble with a low variance can be obtained.[39] Hence, for the correct forecast error covariance to be maintained, a suitable spread of the ensemble members is required. This is achieved by using an ensemble of perturbed observations.[39] An ensemble of the same size q consisting of observations is also generated by adding small perturbations to the observation set $\mathbf{y}_k$. Perturbations are generated to have the same distribution as the measurement error, and the perturbed observations $\mathbf{y}_k^i$ are defined by

$$\mathbf{y}_k^i = \mathbf{y}_k + \mathbf{e}_k^i, \quad i = 1, \dots, q, \tag{5}$$

where $\mathbf{e}_k^i \in \mathbb{R}^p$ is a Gaussian random vector with zero mean and a specified variance. The measurement error covariance matrix, $\mathbf{R_k}$, is diagonal following the assumption of independent observations[33] and is defined as

$$\mathbf{R_k} = \text{diag}\left[\frac{1}{q-1}\mathbf{E}\mathbf{E}^{\mathrm{T}}\right], \quad \mathbf{E} = \left[\mathbf{e}_k^1, \dots, \mathbf{e}_k^q\right]. \tag{6}$$

For a linear measurement function, h, and if the noise is additive, that is,

$$\mathbf{y}_k = \mathbf{H}\mathbf{x}_k + \mathbf{v_k}, \tag{7}$$

the Kalman gain is defined by[36]

$$\mathbf{K_k} = \mathbf{P}_k^{\mathrm{f}}\mathbf{H}^{\mathrm{T}}\left(\mathbf{H}\mathbf{P}_k^{\mathrm{f}}\mathbf{H}^{\mathrm{T}} + \mathbf{R}_k\right)^{-1}. \tag{8}$$

In Equation (8), the observation operator, $\mathbf{H} \in \mathbb{R}^{p\times n}$, is linear or linearized. To circumvent the linearization of a nonlinear measurement function that might be difficult to linearize, Houtekamer and Mitchell[40] rewrote the two terms $\mathbf{P}_k^{\mathrm{f}}\mathbf{H}^{\mathrm{T}}$ and $\mathbf{H}\mathbf{P}_k^{\mathrm{f}}\mathbf{H}^{\mathrm{T}}$ that appear in the Kalman gain Equation (8) as

$$\mathbf{P}_k^{\mathrm{f}}\mathbf{H}^{\mathrm{T}} \equiv \frac{1}{q-1}\sum_{i=1}^{q}\left[\mathbf{x}_k^{\mathrm{f}_i} - \bar{\mathbf{x}}_k^{\mathrm{f}}\right]\left[h\left(\mathbf{x}_k^{\mathrm{f}_i}\right) - \overline{h\left(\mathbf{x}_k^{\mathrm{f}}\right)}\right]^{\mathrm{T}}, \tag{9}$$

$$\mathbf{H}\mathbf{P}_k^{\mathrm{f}}\mathbf{H}^{\mathrm{T}} \equiv \frac{1}{q-1}\sum_{i=1}^{q}\left[h\left(\mathbf{x}_k^{\mathrm{f}_i}\right) - \overline{h\left(\mathbf{x}_k^{\mathrm{f}}\right)}\right]\left[h\left(\mathbf{x}_k^{\mathrm{f}_i}\right) - \overline{h\left(\mathbf{x}_k^{\mathrm{f}}\right)}\right]^{\mathrm{T}}, \tag{10}$$

where $\overline{h\left(\mathbf{x}_k^{\mathrm{f}}\right)} = \frac{1}{q}\sum_{i=1}^{q} h\left(\mathbf{x}_k^{\mathrm{f}_i}\right)$. It has been argued by Tang and Ambadan[41] that Equations (9) and (10) approximately hold, if the following are true:

$$\overline{h\left(\mathbf{x}_k^{\mathrm{f}}\right)} = h\left(\bar{\mathbf{x}}_k^{\mathrm{f}}\right), \tag{11}$$

$$\text{norm}\left(\mathbf{x}_k^{\mathrm{f}_i} - \bar{\mathbf{x}}_k^{\mathrm{f}}\right) \text{ is small for} i = 1, 2, \dots q. \tag{12}$$

Equations (9) and (10) linearize the nonlinear function h to $\mathbf{H}$ under the conditions of Equations (11) and (12).[37] For the nonlinear model with a nonlinear measurement function, a general equation for the Kalman gain can be stated as[37]

$$\mathbf{K}_k = \mathbf{P}_{\mathbf{xy}_k}^{\mathrm{f}}\left(\mathbf{P}_{\mathbf{yy}_k}^{\mathrm{f}}\right)^{-1}, \tag{13}$$

where the error covariance matrices $\mathbf{P}_{\mathbf{xy}_k}^{\mathrm{f}}$ and $\mathbf{P}_{\mathbf{yy}_k}^{\mathrm{f}}$ are defined as follows:

$$\mathbf{P}_{\mathbf{xy}_k}^{\mathrm{f}} = \frac{1}{q-1}\sum_{i=1}^{q}\left[\mathbf{x}_k^{\mathrm{f}_i} - \bar{\mathbf{x}}_k^{\mathrm{f}}\right]\left[h\left(\mathbf{x}_k^{\mathrm{f}_i}\right) - \overline{h\left(\mathbf{x}_k^{\mathrm{f}}\right)}\right]^{\mathrm{T}}, \tag{14}$$

$$\mathbf{P}_{\mathbf{yy}_k}^{\mathrm{f}} = \frac{1}{q-1}\sum_{i=1}^{q}\left[h\left(\mathbf{x}_k^{\mathrm{f}_i}\right) - \overline{h\left(\mathbf{x}_k^{\mathrm{f}}\right)}\right]\left[h\left(\mathbf{x}_k^{\mathrm{f}_i}\right) - \overline{h\left(\mathbf{x}_k^{\mathrm{f}}\right)}\right]^{\mathrm{T}}. \tag{15}$$

We define the **true** state (or parameter) as the **target** of an ideal assimilation. The best forecast state estimate is given by the ensemble mean $\bar{\mathbf{x}}_k^{\mathrm{f}}$. The error between $\bar{\mathbf{x}}_k^{\mathrm{f}}$ and the true state is given by the standard deviation of the ensemble members around $\bar{\mathbf{x}}_k^{\mathrm{f}}$. The final step is the forecast step and involves an ensemble of q forecast states for time $t = k + 1$ as

$$\mathbf{x}_{k+1}^{\mathrm{f}_i} = f\left(\mathbf{x}_k^{\mathrm{a}_i}\right) + \mathbf{w}_k^i, \quad i = 1, 2, \dots q. \tag{16}$$

2.2 | Summary of ensemble Kalman filter algorithm

We now summarize the forecast and analysis steps of EnKF presented in Section 2.1. A schematic description of the EnKF algorithm is shown in Figure 1. To start the EnKF, we need to generate an ensemble of q forecast estimates of state associated with their random errors. At $t = k - 1$, it is assumed that $\mathbf{x}_{k-1}^{\mathrm{f}_i}$ for $i = 1, \dots, q$ are available. We let p denote the number of observations. At time $t = k$ we generate a set of realizations of the state vector $\mathbf{X}_k = (\mathbf{x}_k^1, \dots, \mathbf{x}_k^q)$ and denote the corresponding measurements as $\mathbf{Y}_k = (y_k^1, \dots, y_k^q) \in \mathbb{R}^{q\times p}$. $\mathbf{Q}$ and $\mathbf{R}$ correspond to the model and the observation error covariance matrices, respectively. We write the equations for the EnKF as

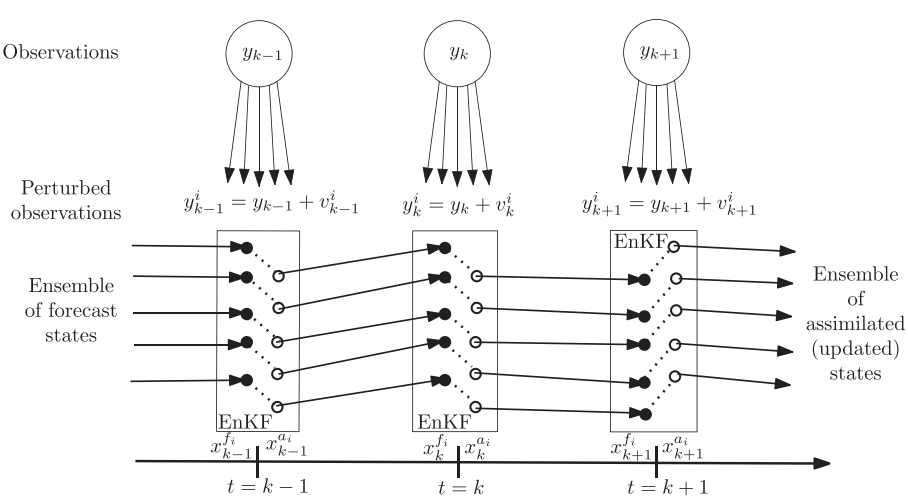

FIGURE 1 A schematic description of the ensemble Kalman filter

$$\mathbf{x}_k^{\mathrm{f}_i} = f\left(\mathbf{x}_{k-1}^{\mathrm{a}_i}\right) + \mathbf{w}_{k-1}^i, \quad i = 1, \dots, q,$$
$$\mathbf{w}_k^i \sim \mathcal{N}(0, \mathbf{Q}_k),$$
$$\mathbf{P}_{\mathbf{xy}_k}^{\mathrm{f}} = \frac{1}{q-1}\sum_{i=1}^{q}\left[\mathbf{x}_k^{\mathrm{f}_i} - \bar{\mathbf{x}}_k^{\mathrm{f}}\right]\left[h\left(\mathbf{x}_k^{\mathrm{f}_i}\right) - \overline{h\left(\mathbf{x}_k^{\mathrm{f}}\right)}\right]^{\mathrm{T}},$$
$$\mathbf{P}_{\mathbf{yy}_k}^{\mathrm{f}} = \frac{1}{q-1}\sum_{i=1}^{q}\left[h\left(\mathbf{x}_k^{\mathrm{f}_i}\right) - \overline{h\left(\mathbf{x}_k^{\mathrm{f}}\right)}\right]\left[h\left(\mathbf{x}_k^{\mathrm{f}_i}\right) - \overline{h\left(\mathbf{x}_k^{\mathrm{f}}\right)}\right]^{\mathrm{T}} + \mathbf{R}_k,$$
$$\mathbf{K}_k = \mathbf{P}_{\mathbf{xy}_k}^{\mathrm{f}}\left(\mathbf{P}_{\mathbf{yy}_k}^{\mathrm{f}}\right)^{-1},$$
$$\mathbf{y}_k^i = \mathbf{y}_k + \mathbf{e}_k^i, \quad i = 1, \dots, q,$$
$$\mathbf{x}_k^{\mathrm{a}_i} = \mathbf{x}_k^{\mathrm{f}_i} + \mathbf{K}_k\left[\mathbf{y}_k^i - h\left(\mathbf{x}_k^{\mathrm{f}_i}\right)\right], \quad i = 1, \dots, q.$$

In the above steps the superscripts 'f' and 'a' denote the forecast and the analysis steps, respectively. EnKF algorithm yields an ensemble of analyses at time $t = k$, which can be cycled in time.

Unscented Kalman filter differs from EnKF by the choice of the sampling. UKF uses a minimal set of deterministically chosen points (sigma points) and propagates this set through the actual nonlinear function.[18] In contrast, EnKF uses a Monte Carlo-based choice of many points (members of the ensemble) for forward propagation. UKF should be preferred, if the output of the system deviates from a Gaussian distribution. Except with the computation of the Kalman gain, all the operations on the ensemble members are independent. This implies that their parallelization can be trivially carried out. This is one of the reasons for the success and popularity of the EnKF and UKF.

3 | PARAMETER ESTIMATION USING ENSEMBLE KALMAN FILTER

In the current work, the EnKF algorithm is used to estimate only the model parameters. The parameters are thus considered as *special state variables* (the state vector contains only the model parameters). The evolution of parameters is characterized by a random walk model[11,12] and is defined as $\mathbf{x}_{k+1}^i = \mathbf{x}_k^i + \tau_k^i$. $\tau_k \sim \mathcal{N}(0, \mathbf{T}_k)$ is a small random perturbation with predefined variance $\mathbf{T}$. Numerical simulators can be regarded as nonlinear functions that take parameter vector $\mathbf{x}^i$ as an input and produce an output vector $\mathbf{y}^i = \mathcal{H}(\mathbf{x}^i)$.[42] $\mathcal{H}$ is the nonlinear measurement function defined by the numerical simulator. The information from observations is used by the Kalman filter during the analysis step, and the Kalman gain Equation (4) is applied to update the ensemble members. The use of Equation (4) assumes that the parameters follow a Gaussian distribution.[42] The parameter estimation procedure using the EnKF is stated in Algorithm 1.[42] The algorithm can be stopped when some finite convergence criterion is achieved. A flowchart for parameter estimation using EnKF is shown in Figure 2. Positivity issues are physically important but often difficult to enforce in assimilation processes. In this study the parameters (e.g., the Young's modulus) need to remain positive. To avoid negative values of the Young's modulus during the assimilation procedure, we introduce a change of variable. More precisely, in the sequel all the parameters are redefined as $x = x_{ref}2^{\theta}$. x is the real parameter (e.g., the Young's modulus), θ is the parameter used for estimation in EnKF, and x_{ref} is a reference value (initial mean value for the Young's modulus). With this change of variable, the values of estimated parameters remain positive.[18] The EnKF implementation uses an ensemble of θ such that $\theta \sim \mathcal{N}(0, 1)$.

4 | THE BLOOD FLOW MODEL

We first recall the 1D governing equations for the blood flows in variables u (cross-section averaged blood velocity), A (cross-section area), and p (cross-section averaged static pressure), which have been widely used in hemodynamics applications.[24,43–52] 1D modeling of arterial networks being computationally cheap is a common method adopted to perform numerical simulations of the hemodynamics in arterial vessels.[47,53] The model assumes that blood is a Newtonian fluid in large vessels and can be considered incompressible with constant density ρ and constant dynamic viscosity μ.[50]

4.1 | Governing equations

For an incompressible and Newtonian fluid in an elastic tube, the system of equations that represents continuity of mass and momentum can be stated as[43]

$$\begin{aligned} \frac{\partial A}{\partial t} + \frac{\partial q}{\partial x} &= 0, \\ \frac{\partial q}{\partial t} + \frac{\partial}{\partial x}\left(\alpha\frac{q^2}{A}\right) + \frac{A}{\rho}\frac{\partial p}{\partial x} &= -k_r\frac{q}{A}, \end{aligned} \tag{17}$$

where x is the axial direction, $A = A(x,t)$ is the cross-section area at time t, $q = q(x, t)$ is the flow rate across a section, ρ is the constant density of the blood, p is the cross-section average static internal pressure, and $u(x, t) = \frac{q(x,t)}{A(x,t)}$ denotes the cross-section averaged blood velocity. The term α is the momentum-flux correction coefficient. For a flat velocity profile, it is assumed that $\alpha = 1$.[43] k_r denotes the viscous resistance of the flow per unit length of the tube. A, q, and p are the unknowns in the system (17). The system is closed by explicitly providing a differential constitutive pressure-area relationship.[43] A nonlinear model for pressure law is adopted according to Kelvin-Voigt model[24]:

$$p = p_{ext} + \frac{\beta}{A_0}\left[\left(\sqrt{A} - \sqrt{A_0}\right) + \epsilon_p\left(\sqrt{A} - \sqrt{A_0}\right)^2\right] + \frac{\gamma}{A_0}\frac{\partial\sqrt{A}}{\partial t}, \tag{18}$$

where p_{ext} denotes the constant external pressure, $A_0 = A_0(x)$ denotes the vessel sectional area at equilibrium state, and ϵ_p is the nonlinearity coefficient. The term γ is $h\eta\sqrt{\pi}$, where h is

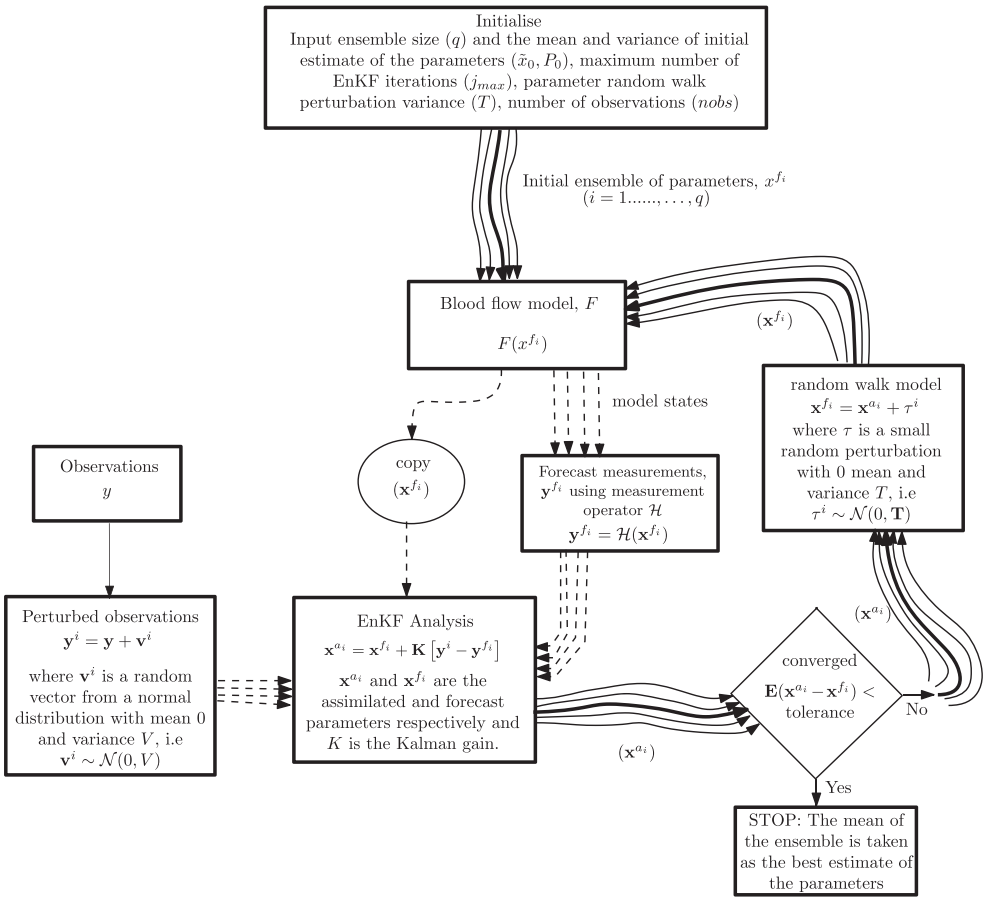

FIGURE 2 Parameter estimation flowchart using the ensemble Kalman filter

the thickness of the tube and η is the viscoelastic coefficient. The coefficient β, which is related to the arterial stiffness, is defined as

$$\beta = \frac{\sqrt{\pi} h E}{\left(1 - \sigma^2\right)}, \tag{19}$$

where $E = E(x)$ is the Young's modulus and $\sigma = 0.5$ is the Poisson ratio.[43]

With a specified inflow boundary condition, the 1D governing equations for the blood flow are solved using the terminal models for the outflow boundary conditions.[47]

4.2 | Characteristic variables

The 1D model (17) can be rewritten in a conservative form,

$$\frac{\partial \mathbf{U}}{\partial t} + \frac{\partial \mathbf{F}(\mathbf{U})}{\partial x} = \mathbf{S}(\mathbf{U}), \tag{20}$$

where $\mathbf{U} = [A, q]^T$ denotes the vector of conserved variables, $\mathbf{F}(\mathbf{U})$ are the fluxes, and $\mathbf{S}(\mathbf{U})$ are the source terms defined by

$$\mathbf{F}(\mathbf{U}) = \begin{bmatrix} q \\ \alpha \frac{q^2}{A} + \frac{\beta}{3\rho A_0} A^{\frac{3}{2}} + \frac{\beta \epsilon_p}{\rho A_0}\left(\frac{1}{2}A^2 - \frac{2}{3}\sqrt{A_0} A^{\frac{3}{2}}\right) \end{bmatrix},$$
$$\mathbf{S}(\mathbf{U}) = \begin{bmatrix} 0 \\ -k_r \frac{q}{A} + \frac{\gamma\sqrt{A}}{2\rho A_0}\left(\frac{\partial^2 q}{\partial x^2} - \frac{1}{2A}\frac{\partial A}{\partial x}\frac{\partial q}{\partial x}\right) \end{bmatrix}. \tag{21}$$

The highly coupled system of nonlinear equations (20) is decoupled to implement the numerical solution with the prescribed boundary conditions.[46] The characteristic system is derived by expressing the system of equations (20) in a quasi-linear form which can be expressed as[46]

$$\frac{\partial \mathbf{U}}{\partial t} + \mathbf{J}\frac{\partial \mathbf{U}}{\partial x} = \mathbf{S}, \tag{22}$$

where the Jacobian reads

$$\mathbf{J}(\mathbf{U}) = \frac{\partial \mathbf{F}}{\partial \mathbf{U}} = \begin{bmatrix} 0 & 1 \\ -\alpha \frac{q^2}{A^2} + \frac{\beta}{2\rho A_0} A^{\frac{1}{2}} + \frac{\beta \epsilon_p}{\rho A_0}\left(A - \sqrt{A_0}\sqrt{A}\right) & 2\alpha \frac{q}{A} \end{bmatrix}. \tag{23}$$

Through consideration of the nonlinear coefficient (ϵ_p) and visco elasticity (η) as source terms, the characteristic analysis shows that, for all allowable $\mathbf{U}$ (that is for $A > 0$), the system is hyperbolic and the two real eigenvalues of $\mathbf{J}$ are[48,49]

$$\lambda_1 = \frac{\alpha q}{A} + \sqrt{\frac{\beta}{2\rho A_0} A^{\frac{1}{2}} + \alpha(\alpha - 1)\frac{q^2}{A^2}} > 0,$$
$$\lambda_2 = \frac{\alpha q}{A} - \sqrt{\frac{\beta}{2\rho A_0} A^{\frac{1}{2}} + \alpha(\alpha - 1)\frac{q^2}{A^2}} < 0. \tag{24}$$

When $\alpha = 1$, the associated characteristic variables have the following expressions:

$$W_1 = \frac{q}{A} + 4(c - c_0),$$
$$W_2 = \frac{q}{A} - 4(c - c_0), \tag{25}$$

where $c = \sqrt{\frac{\beta}{2\rho A_0}} A^{\frac{1}{4}}$ and $c_0 = \sqrt{\frac{\beta}{2\rho A_0}} A_0^{\frac{1}{4}}$. The characteristic system can be expressed as the decoupled system of equations:

$$\frac{\partial w_1}{\partial t} + \lambda_1 \frac{\partial w_1}{\partial x} = 0,$$
$$\frac{\partial w_2}{\partial t} + \lambda_2 \frac{\partial w_2}{\partial x} = 0. \tag{26}$$

The wave velocity that arises from the blood wall coupling may take values as low as 5m/s in large arteries (e.g., aorta), increasing to values around 20-35m/s in less distensible peripheral arteries.[50] However, peak flow velocities u are much smaller and usually remain less than around 1m/s.

4.3 | Numerical approximation

Several methods have been used,[43–45,52,54] for the numerical approximation of the 1D system of conservation laws (17). In this section we follow Peiró and Veneziani (2009)[45] and Formaggia et al. (2003),[54] where equations of the 1D model are discretized in their conservative form (20) by employing a second-order Taylor Galerkin scheme. We denote $\triangle t = t^{n+1} - t^n$ the time step and express the Taylor expansion truncated to the second order at time t^n, giving

$$\mathbf{U}^{n+1} = \mathbf{U}^n + \triangle t \frac{\partial \mathbf{U}}{\partial t}\bigg|^n + \frac{\triangle t^2}{2} \frac{\partial^2 \mathbf{U}}{\partial t^2}\bigg|^n. \tag{27}$$

We define the matrix

$$\mathbf{K} = \frac{\partial \mathbf{S}}{\partial \mathbf{U}} = \begin{bmatrix} 0 & 0 \\ k_r \frac{q}{A^2} + \frac{\gamma}{4\rho A_0} \frac{1}{\sqrt{A}} \left(\frac{\partial^2 q}{\partial x^2} + \frac{1}{2A} \frac{\partial A}{\partial x} \frac{\partial q}{\partial x} \right) & -\frac{k_r}{A} \end{bmatrix} \tag{28}$$

and rewrite (20) as

$$\frac{\partial \mathbf{U}}{\partial t} = \mathbf{S} - \frac{\partial \mathbf{F}}{\partial x}. \tag{29}$$

Using the matrices (23) and (28), we obtain

$$\begin{aligned} \frac{\partial^2 \mathbf{U}}{\partial t^2} &= \frac{\partial \mathbf{S}}{\partial \mathbf{U}} \frac{\partial \mathbf{U}}{\partial t} - \frac{\partial}{\partial x} \left(\frac{\partial \mathbf{F}}{\partial \mathbf{U}} \frac{\partial \mathbf{U}}{\partial \mathbf{t}} \right) \\ &= \mathbf{K} \frac{\partial \mathbf{U}}{\partial \mathbf{t}} - \frac{\partial}{\partial x} \left(\mathbf{J} \frac{\partial \mathbf{U}}{\partial \mathbf{t}} \right) \\ &= \mathbf{K} \left(\mathbf{S} - \frac{\partial \mathbf{F}}{\partial x} \right) - \frac{\partial (\mathbf{JS})}{\partial x} + \frac{\partial}{\partial x} \left(\mathbf{J} \frac{\partial \mathbf{F}}{\partial \mathbf{x}} \right). \end{aligned} \tag{30}$$

At time $t^n = n\triangle t$, the vector of unknowns $\mathbf{U}^n$ satisfies the following time marching scheme:

$$\begin{aligned} \mathbf{U}^{n+1} = \mathbf{U}^n + \triangle t \left(\mathbf{S}^n - \frac{\partial \mathbf{F}^n}{\partial x} \right) + \frac{\triangle t^2}{2} \\ \times \left(\mathbf{K}^n \left(\mathbf{S}^n - \frac{\partial \mathbf{F}^n}{\partial x} \right) - \frac{\partial (\mathbf{J}^n \mathbf{S}^n)}{\partial x} + \frac{\partial}{\partial x} \left(\mathbf{J}^n \frac{\partial \mathbf{F}^n}{\partial x} \right) \right). \end{aligned} \tag{31}$$

The spatial discretization uses linear finite elements. The domain Ω is subdivided into N_{el} finite elements Ω_e of size h_e. We let V_h be the set of continuous vector functions in Ω, linear on each element and V_h^0 the subspace of V_h whose functions are 0 at the endpoints.[45] The solution of (31) requires, for $n \geq 0$, to determine $\mathbf{U}^{n+1}$ in V_h such that $\forall \phi_h \in V_h^0$,

$$\begin{aligned} \left(\mathbf{U}^{n+1}, \phi_h \right) = (\mathbf{U}^n, \phi_h) + \triangle t \left(\mathbf{S}^n, \phi_h \right) + \triangle t \left(\mathbf{F}^n, \frac{\partial \phi_h}{\partial x} \right) \\ + \frac{\triangle t^2}{2} \left(\mathbf{K}^n \left(\mathbf{S}^n - \frac{\partial \mathbf{F}^n}{\partial x} \right), \phi_h \right) \\ + \frac{\triangle t^2}{2} \left(\mathbf{J}^n \left(\mathbf{S}^n - \frac{\partial \mathbf{F}^n}{\partial x} \right), \frac{\partial \phi_h}{\partial x} \right), \end{aligned} \tag{32}$$

where $(\mathbf{U}, \phi) = \int_0^L \mathbf{U}.\phi dx$.

For the stability of the numerical method, we follow Formaggia et al. (2003)[54] and impose the following limitation for the time step

$$\triangle t \leq \text{CFL} \times \min_{0 \leq i \leq N_{el}} \left[\frac{h_i}{\max(\lambda_{1,i} \lambda_{1,i+1})} \right], \tag{33}$$

where $\lambda_{1,i}$ is the value of λ_1 at mesh node x_i and the maximum CFL number is $\frac{\sqrt{3}}{3}$.[54]

4.4 | Initial and boundary conditions

The initial conditions for (31) are given by

$$A(x, 0) = A_0(x), \quad q(x, 0) = 0, \quad p(x, 0) = p_0(x), \tag{34}$$

where $A_0(x)$ and $p_0(x)$ are the prescribed functions. The hyperbolic nature of the system permits to impose the flow rate q or area A at the inlet.[43] At the inlet usually, the flow rate is specified,[55]

$$q(0, t) = q_{\text{in}}(t). \tag{35}$$

Information from the outside and inside of the domain is carried by the incoming characteristic (W_1) and the outgoing characteristics (W_2), respectively.[44]

At each end of the tube, a single boundary condition is implemented. This is due to the characteristic analysis and using the fact that the flow is subcritical (the eigenvalues [$\lambda_1$and λ_2] in (24) have opposite signs) under physiological conditions.[43,51] At the inlet at $x = 0$, $\mathbf{U}^n$ is assumed to be known and λ_2 in (26) is linearized by taking its value at time t^n. It can be shown that, at the time t^{n+1}, the solution corresponding to this linearized problem yields[43,46]

$$W_2^{n+1}(0) = W_2^n(-\lambda_2^n(0) \triangle t). \tag{36}$$

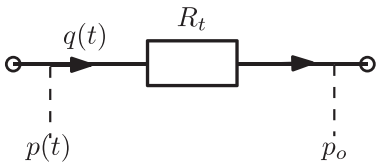

FIGURE 3 A constant resistance model representing an outflow boundary condition

Equation (36) is a first-order extrapolation of W_2 from the previous time step. Similar treatment at the outlet $x = L$ leads to

$$W_1^{n+1}(L) = W_1^n(L - \lambda_1^n(L) \triangle t). \tag{37}$$

4.5 | Terminal vessels

For reduction of the complexity of the blood flow simulation, smaller arteries, which are downstream of the truncation points, are not explicitly accounted for but their effect is represented by proper outflow boundary conditions.[56] The two most common models used are the *constant resistance model*[24,44,46,56,57] and the *Windkessel model*,[52,56,57] which can be obtained using an analogy based on electric circuit components.

The constant resistance model (see Figure 3) is represented by a resistor R_t,[56] where it is assumed that the blood pressure, $p(t) - p_0$, is proportional to the blood flow rate $q(t)$. The relation between the blood pressure and the flow is given by $p(t) - p_0 = R_t q(t)$, where R_t represents the terminal reflection coefficient. The terminal reflection coefficient for a wavefront traveling in the $+x$ direction can be defined in terms of the incoming and outgoing characteristics as[44,46]

$$R_t = -\frac{\triangle W_2}{\triangle W_1} = -\frac{W_2^{n+1} - W_2^0}{W_1^{n+1} - W_1^0}. \tag{38}$$

The values for W_1^{n+1} are determined using Equation (37), whereas W_1^0 and W_2^0 are the initial values.[46] The unknown W_2^{n+1} is determined by rearranging Equation (38), giving

$$W_2^{n+1} = W_2^0 - R_t\left(W_1^{n+1} - W_1^0\right). \tag{39}$$

A reflection coefficient of $R_t = 0$ represents a nonreflecting boundary condition.

4.6 | Treatment of bifurcations

At bifurcation of a blood vessel, we assume that pressure losses are negligible. We follow[44] and enforce the following conditions:

$$\begin{aligned} &\sum_{i=1}^{3} q_i = 0, \frac{1}{2}\rho\left(\frac{q_1}{A_1}\right)^2 \\ &\quad + p_1 - \frac{1}{2}\rho\left(\frac{q_i}{A_i}\right)^2 - p_i \quad = 0, \quad i = 2, 3, \end{aligned} \tag{40}$$

representing the conservation of flow rate and total pressure continuity equations, respectively.

5 | APPLICATION OF ENKF TO 1D BLOOD FLOW MODEL

In this section we present the use of the EnKF algorithm to solve the parameter estimation problem in a series of test cases. The first two tests are purely *in silico*. That is, we use only synthetic data (observations) that are obtained from a forward simulation, where the model parameters are set to some known or target values. From these observations the parameter estimation problem then starts with an initial estimate for the parameters that differs significantly from the target values. With synthetic data an inverse problem is always admissible, when the objective is to recover the target parameters. By admissible we mean that because the target is generated with the model, the solution of the inversion targeting this results obviously exists, but still there is no guarantee of uniqueness. Indeed, regardless of existence of solution that is guaranteed in this case, several distributions of the parameters could achieve the target. The final test case uses data from the experiment performed by Saito et al.[24] In this latter case, unlike with the synthetic data, there is no guarantee that the solution to the inverse problem actually exists.

In Saito (2011),[24] a simple human arterial network was designed using polymer tubes to validate the applicability of the 1D blood flow model. The network was made with 4 bifurcations and consisted of the main artery, a left carotid artery, femoral arteries (left and right), and subclavian-radial arteries (left and right). The schematic of this simple human arterial model is shown in Figure 4 and the geometry of the arteries (length, diameter, and the thickness) in Table 1.[24]

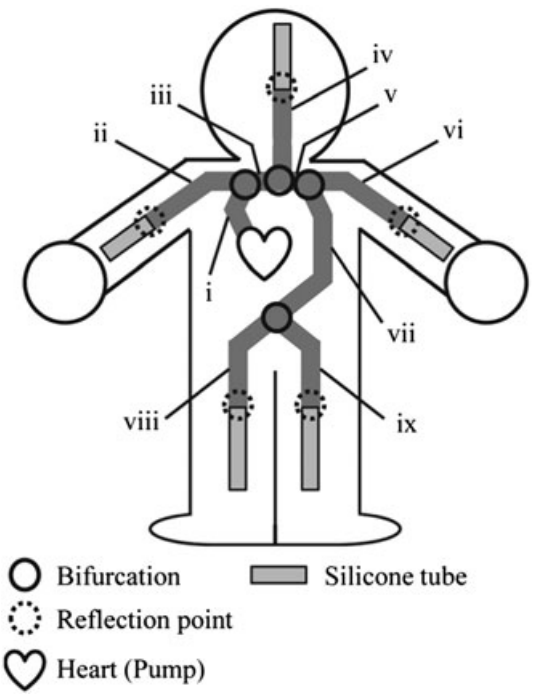

FIGURE 4 Schematic of a simple human arterial model with 9 vessels and 4 bifurcations. Artery numbers correspond to those in Table 1. Figure adapted from Saito et al.[24]

TABLE 1 Geometrical data (L = length, D = diameter, and h = thickness) of a simple human arterial model (Figure 4)[24]

	Name	L (mm)	D (mm)	h (mm)
i	Aorta arch A	35	12	2
ii	R. subclavian radial artery	800	6	1.5
iii	Aorta arch B	20	11	2
iv	L. carotid artery	675	6	1.5
v	Aorta arch C	40	10	2
vi	L. Subclavian radial artery	710	6	1.5
vii	Aorta	470	8	1.5
viii	R. femoral artery	365	6	1.5
ix	L. femoral artery	365	6	1.5

An appropriate length of blood vessels was defined according to the vessel data of an average adult man. The diameter and thickness were defined to achieve a negligible reflection coefficient at bifurcation point.[24] For all test cases we use the simple arterial model as in Figure 4. We limit our parameters of interest to Young's modulus and terminal model parameters (reflection coefficient), which are within a physiological range.

5.1 | Two test cases with synthetic data

One of the important parameters for EnKF is q, the ensemble size. It is expected that the EnKF parameter estimation procedure would improve as the ensemble size increases. The increase in an ensemble size will also increase the computational cost associated with it. In our test cases we assume that the blood flow model errors and uncertainties arise from the errors in the parameters, and thus, an ensemble is generated with perturbed parameters. As detailed in what follows, we therefore performed a parametric study to select a proper ensemble size.

We first simulate the blood flow model using an arbitrary set of parameters $\{E, R_t\}$. The resulting simulated model states are stored as $p^{\text{sim}} \in \mathbb{R}^n$. An ensemble of size q is generated where the ensemble members are $\left\{E', R_t'\right\}_i$ for $i = 1 \ldots, q$. For each i, E' is a random normal variable with mean E and standard deviation of $0.1E$. Similarly, R_t' is a random normal variable with mean R_t and standard deviation of $0.1R_t$. The blood flow model is then simulated with each member of the ensemble, and the observed pressure values at the end of the simulation are stored as $p^{obs_i} \in \mathbb{R}^n$. To select an ensemble size for the EnKF analysis, we calculated the root mean square error defined for each member of the ensemble as $\text{RMSE}_i = \sqrt{\frac{1}{n}\sum_{j=1}^{n}\left(p_j^{sim} - p_j^{obs_i}\right)^2}$. Finally, we find the mean RMSE for the ensemble of size q as $\text{RMSE} = \frac{1}{q}\sum_{i=1}^{q}\text{RMSE}_i$. The procedure was repeated with different ensemble sizes between $q = 2$ and $q = 60$. From Figure 5, which shows the output of the procedure with different random seeds, the mean RMSE decreases sharply initially with q increasing. From this figure the error does not decrease after $q \approx 20$ and this latter value was thus retained in the present study.

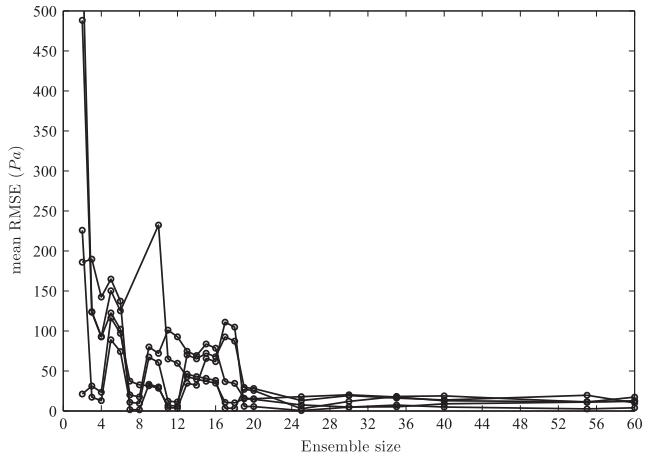

FIGURE 5 Mean RMSE as a function of ensemble size. Five sets of RMSE are calculated with different random seeds

5.1.1 | Test case 1:

The first test case deals with the estimation of the Young's modulus for a single artery. We first describe the procedure for generating the synthetic data. All arteries except aorta (number vii in Figure 4) is assigned a Young's modulus of 0.2 MPa, and to aorta (number vii), we assigned 0.25MPa assuming some pathology there locally increasing its stiffness. A contant resistance model is applied to the terminal vessels. A reflection coefficient of $R_t = 0.6$ is assigned to the terminal vessels ii, iv, and vi and for terminal vessels vii and ix, $R_t = 0.65$. Figure 6 shows the periodic inlet flow rate boundary condition $q_{\text{in}}(t)$ (with a period of 0.8s and an average inlet flow of 5.625 mL/s) imposed at the aorta arch A of the simple arterial model. The density of the fluid is taken as 1.0 kg/m^3, the viscosity of 1×10^{-3} Pa.s, and the Poisson's coefficient is taken as 0.5. The viscoelastic coefficient η and the nonlinearity coefficient ϵ_p of the vessel are set to 0 for the forward simulation. The time step for the forward simulation is 0.1 ms, corresponding to $CFL = 0.05$. Synthetic pressure observations are taken at every 0.01s. The first objective is to determine the minimum number of observations ($nobs$), needed for a proper parameter estimation. $nobs$ refers to the number of locations where a time series of pressure is available. Other time series can be considered and we will present also simulations with flow rate time series in Section 5.1.2. Algorithm 1 is executed initially with $nobs = 6$; $nobs$ is then decreased in steps of one to a minimum of 1. These observations are assumed to be available from the left and right subclavian radial arteries (artery # ii and vi) and the left carotid artery (artery # iv). The locations of these observations are shown in Table 2.

For the estimation problem, the Young's modulus is sought for the stiffest aorta, denoted by vii in Figure 4. An ensemble of $q = 20$ members is considered in all the cases. For each member of the ensemble, the observations are perturbed

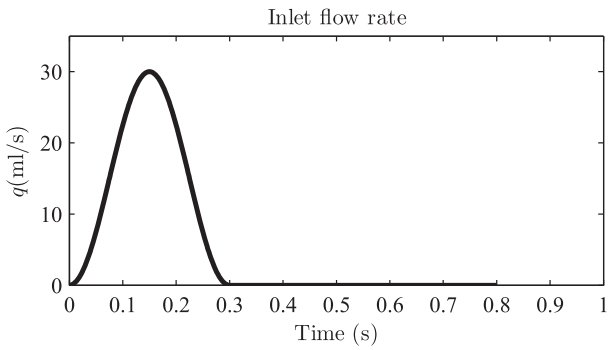

FIGURE 6 Periodic inlet flow rate $q_{in}(t)$ imposed at the aorta arch A

by a random vector drawn from the zero mean Gaussian distribution with a standard deviation at 5% of the observation value. We compute the measurement error covariance matrix **R** using Equation (6). The initial guess for the Young's modulus assumes an error of 100%, ie, initial mean value for $E =$ 0.5MPa.

is no guarantee that the first search iterations are performed in a direction (in parameter space) pointing toward a minimum of the error. This behavior also comes from the fact that the method is by nature explicit, as in a gradient-based methods. Table 3 shows the value of estimated Young's modulus with errors (percentage deviation from target value) using different number of observations. The percentage deviations from target E were all less than 5%. For this test case, a minimum of 1 observation was enough to recover the Young's modulus requested in the given interval of time. In Figure 7B, the pressure solutions obtained by using the estimated Young's modulus at the first observation point on left carotid are compared with the target and the initial guessed pressure profiles. The comparison is shown for Young's modulus estimated using $nobs =$ 2. Even though the solution in the vessel whose Young's modulus is sought for is not directly observed, the simulated pressure waveforms are similar in shape to the target pressure waveform with an error of less than 0.2% in the maximum pressure.

Algorithm 1: Parameter estimation using EnKF

Input: Ensemble size (q), maximum number of EnKF iteration (j_{max}), variance matrix $\mathbf{T}$, number of observations ($nobs$), initial guess of the parameters (mean $\tilde{\mathbf{x}}_0$ and covariance $\mathbf{P}_0$).

Initialization:

Initialize randomly q states into special state matrix $\mathbf{X}$

for $j = 1$ ***to*** j_{max} **do**

  -Perturb the ensemble using random walk model

  $\mathbf{x}^{\mathrm{f}_i} = \mathbf{x}^{\mathrm{a}_i} + \tau^i, \tau^i \sim \mathcal{N}(0, \mathbf{T}) \;\; \forall i = 1, \ldots, q$

  -Propagate the ensemble

  $\mathbf{y}^{\mathrm{f}_i} = \mathcal{H}(\mathbf{x}^{\mathrm{f}_i}) \;\; \forall i = 1, \ldots, q$

  -Perturb the observations for each ensemble

  $\mathbf{y}^i = \mathbf{y} + \mathbf{e}^i, \;\; \forall i = 1, \ldots, q$

  -Update the ensemble

  Estimate $\mathbf{R}$ using Eq. (6) and Kalman gain, $\mathbf{K}$, using Eq. (13, 14 and 15)

  $\mathbf{x}^{\mathrm{a}_i} = \mathbf{x}^{\mathrm{f}_i} + \mathbf{K}\left[\mathbf{y}^i - \mathbf{y}^{\mathrm{f}_i}\right] \;\; \forall i = 1, \ldots, q.$

The parameter estimation using Algorithm 1 is then performed with different numbers of observations, *nobs*. The EnKF assimilation is executed for 10s and the evolution of the estimated Young's modulus is shown in Figure 7A. It appears that convergence only takes place after some time. This kind of trend is often observed in optimization, especially with methods involving a learning feature. Indeed, there

5.1.2 | Sensitivity analysis:

In this section we look at the sensitivity of the parameter estimation algorithm for test case 1 with respect to the following items: (i) initial estimate of the parameter, (ii) level of observation perturbation, (iii) the effect of introducing bias in the known parameter values, and (iv) the observation type.

TABLE 2 Location of observations on right subclavian radial artery (ii), left carotid artery (iv), and left subclavian artery (vi) for synthetic test cases

Artery #	*nobs* = 1	*nobs* = 2	*nobs* = 3	*nobs* = 4	*nobs* = 5	*nobs* = 6
ii		0.25*L*	0.25*L*	0.25*L*	0.25*L*, 0.75*L*	0.25*L*, 0.75*L*
iv	0.2*L*	0.2*L*	0.2*L*	0.2*L*, 0.8*L*	0.2*L*	0.2*L*, 0.8*L*
vi			0.33*L*	0.33*L*	0.33*L*, 0.67*L*	0.33*L*, 0.67*L*

where *L* is the length of the artery.

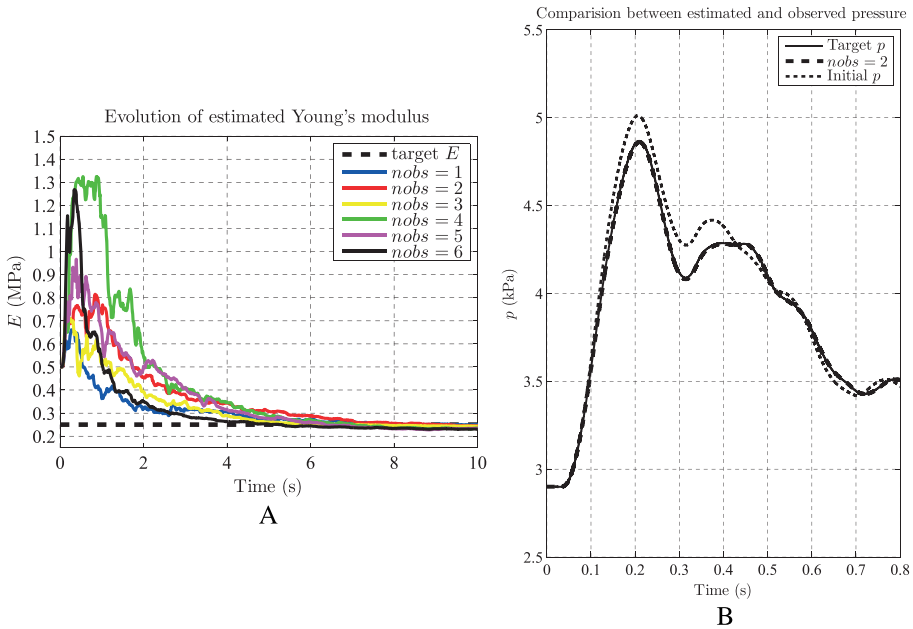

FIGURE 7 (A) The evolution of the estimated Young's modulus using ensemble Kalman filter for test case 1 using a different number of observations. The initial value is 0.5MPa and the target is 0.25MPa. (B) The comparison between target pressure solution, the initial pressure profile, and the one obtained by using the estimated Young's modulus with *nobs* = 2 at 0.2*L* of the left carotid artery.

TABLE 3 Test case 1: Estimated Young's modulus and corresponding errors (percentage deviation from target value) using different number of observations

	nobs = 1	*nobs* = 2	*nobs* = 3	*nobs* = 4	*nobs* = 5	*nobs* = 6
Estimated *E*(MPa)	0.239	0.245	0.243	0.245	0.241	0.246
% deviation from target *E*	− 4.49	− 1.95	− 2.64	− 1.82	− 3.52	− 1.79

- *Initial guess*: We study the performance of EnKF by considering different initial values of the Young's modulus for the parameter estimation problem. Two more initial values of $E = 0.15$ (− 40% error) and 0.35MPa (+40% error) were taken as the mean values of the initial ensembles. All other parameters and settings were the same as in Section 5.1.1. Using *nobs* = 2, the EnKF assimilation is executed for 10s and the evolution of estimated Young's modulus with their uncertainty (standard deviations) is shown in Figure 8(a) for 3 different initial values, including for $E = 0.5$ MPa (+100% error). The algorithm allows retrieving the target value independently on the initial guess. Table 4 compares the initial and final estimates of the Young's modulus with their associated uncertainties.
- *The level of observation perturbation*: As in Section 2.1, the observations are perturbed by Gaussian noises. The noises represent possible errors in the measurement. For unbiased observations, perturbed observations are created by adding noise ($\sim (\mathcal{N}(0, \sigma^2))$, to the observation values; σ represents the standard deviation. In test case 1, σ equals 5% of observation values, and for the analysis, we chose 2 more levels of observation perturbations with σ being 1% and 10% of observations values, respectively. Using *nobs* = 2, we perform the estimation procedure for 10s. The estimated Young's modulus with their uncertainty (standard deviations) are shown in Figure 8B for the 3 different levels of observation perturbations. With different values of σ, the estimated E's converge to the target value, but with a slightly different rate. With a lower σ (at 1% of observation values) the convergence rate is a little slower compared with the other two σ's, which was not anticipated. Table 5 compares the initial and final estimates of the Young's modulus with their uncertainties for the different level of perturbations used.

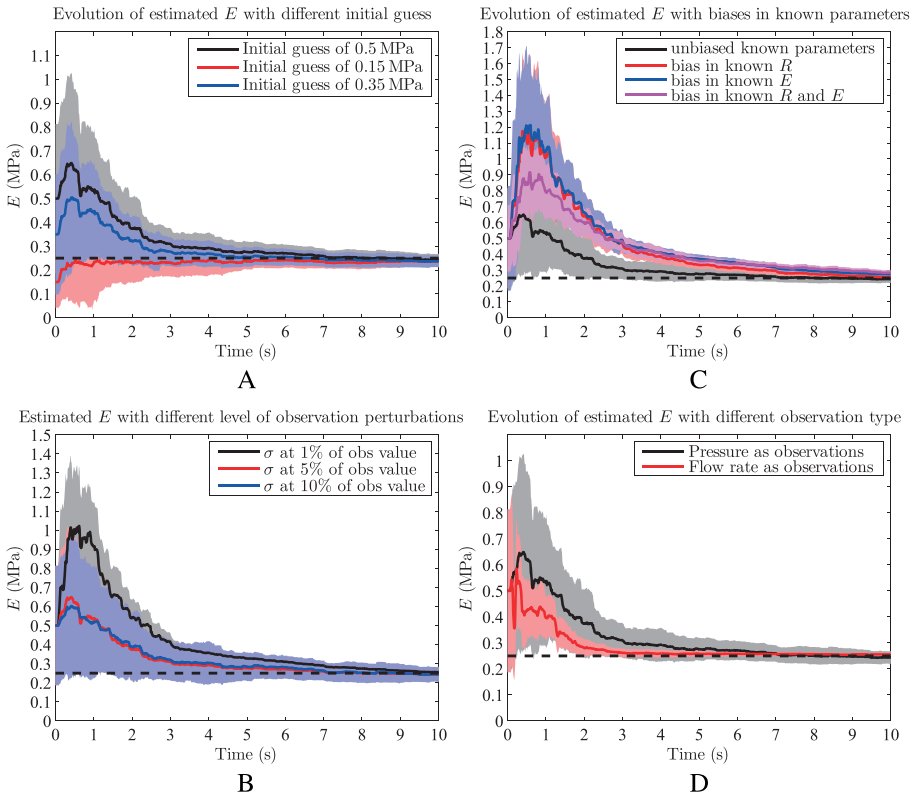

FIGURE 8 Sensitivity analysis for test case 1. In all the figures, the dashed line represents the target Young's modulus of 0.25MPa and the shaded areas represents the standard deviation around the mean values (solid lines). (A) The evolutions of the estimated Young's modulus from 3 different initial values. (B) The evolution of estimated Young's modulus for 3 different levels of observation perturbations. (C) The evolution of the estimated Young's modulus for different bias in the known parameters: R_t perturbed with Gaussian noises having mean 0 and a standard deviation at 5% of the values of R_t (in red), E randomly perturbed with Gaussian noises having mean 0 and a standard deviation at 10% of the values of E (in blue), both E and R_t randomly perturbed with Gaussian noises having mean 0 and a standard deviation at 5% of the values of R_t and 10% of the values of E (in magenta). The evolution of estimated E with unbiased known parameters is shown in black. (D) The evolution of the estimated Young's modulus with pressure and flow rates as observation types.

TABLE 4 Sensitivity with different initial values: final estimates of Young's modulus with their associated uncertainties

Initial guess of E	Final estimate of E	Uncertainty (± standard deviation)
0.15	0.2367	0.0228
0.35	0.2370	0.0250
0.50	0.2450	0.0245

All values are in megapascal.

TABLE 5 Sensitivity with different level of observation perturbation: the initial guess of $E = 0.5$MPa and the final estimates of Young's modulus with their associated uncertainties are shown below

σ	Final estimate of E	Uncertainty (± standard deviation)
1% of observation values	0.2556	0.0122
5% of observation values	0.2450	0.0245
10% of observation values	0.2441	0.0398

Perturbed observations are created by adding noise ($\sim (\mathcal{N}(0, \sigma^2))$, to the observation values. All values of E and standard deviation are in megapascal.

- *Bias in the known parameter values*: In test case 1, we estimated the Young's modulus for artery # vii assuming that we know the values of E for all other arteries. We also assumed that all reflection coefficients were known. The performance of the estimation algorithm was tested by introducing biases in the known values of E and R_t. Three different test were carried out as follows: (i) We randomly perturbed the values of reflection coefficients, R_t, with Gaussian noises having mean 0 and a standard deviation at 5% of the values of R_t. (ii) The known values of Young's modulus, E, are randomly perturbed with Gaussian noises having mean 0 and a standard deviation at 10% of the values of E. (iii) Known values of both reflection coefficients and Young's modulus are randomly perturbed with Gaussian noises having mean 0 and a standard deviation at 5% of the values of R_t and 10% of the values of E. Pressure values in space were used as observations with the level of observation perturbation set at 5% of observation values and the estimation procedure is executed for 10s. For all tests the initial value of E assumes an error of 100%. The evolution of the estimated Young's modulus with their uncertainties for 3 different tests is shown in Figure 8C together with the evolution of estimated E when known Young's modulus and reflection coefficients are unbiased. For all the cases the estimated values converge but they slightly deviate from the target value as reported in Table 6, which also gives indications of the level of uncertainties in these inversions.

TABLE 6 Sensitivity test: bias in the known parameter values

Random perturbation of known values of parameters by adding noise ($\sim (\mathcal{N}(0, \sigma^2))$.	Final estimate of E	Uncertainty ($\pm$ standard deviation)
unperturbed known parameters values	0.2450	0.0245
σ is 5% of R_t values	0.2580	0.0132
σ is 10% of E values	0.2752	0.0129
σ is 5% of R_t values and 10% of E values	0.2480	0.0161

The initial guess of $E =$ 0.5MPa and the final estimates of Young's modulus with their associated uncertainties are shown. All values of E and standard deviation are in megapascal.

- *Observation type*: In inverse hemodynamics problems, observations such as blood pressure, cross-section blood flow rates, artery wall movements, or cross-section flow velocity can be made available. In test case 1, the observations are pressure values histories at some specific locations in space. The behavior of the estimation algorithm with different kinds of observations. To this end, we consider the flow rate in space as observations instead of the pressure. We perform the estimation procedure for 10s using $nobs =$ 2 with the level of observation perturbation set at 5% of the observed values. We compare these results to those obtained with the pressure as observation. The evolution of estimated Young's modulus with the associated uncertainties is shown in Figure 8D. With both types of observations, the estimated Young's modulus converges to the target value with relatively small errors (-1.95% and $+2.24\%$ with pressure and flow rate as observations, respectively). However, when the observations are based on the flow rates, the convergence is slightly faster, at least in this particular case. The final estimates of E is 0.2450 ± 0.0245MPa when the pressure is considered as the observed quantity. On the other hand, with the flow rate as observation, the final estimate of E is 0.2556 ± 0.0059 MPa.

5.1.3 | Test case 2:

The second test case deals with the estimation of the Young's modulus of all the arteries (i-ix) and the reflection coefficient at all the outlet boundaries (ii, iv, vi, vii, and ix). All arteries are assumed to have the identical stiffness, and thus, a Young's modulus of $E = 0.2$MPa is assigned to all. A reflection coefficient of $R_t =$ 0.6 is assigned at all terminal vessels. The viscoelastic coefficient η and the nonlinearity coefficient ϵ_p of the vessels are set to 0.115kPa.s and 0, respectively, for the forward simulation. The rest of the parameters are as in Section 5.1.1. For the estimation problem, the Young's modulus of the arteries and the reflection coefficient at terminal arteries are sought using various numbers of observations. The ensemble size q and the error covariance matrix $\mathbf{R}$ are as in Section 5.1.1. The mean values for the initial guess of the Young's modulus and the reflection coefficient are set to $E =$ 0.4 MPa and $R_t = 0.8$. The EnKF assimilation is executed for 12s and the evolution of estimated E and R_t is shown in Figure 9A,B, respectively, for the different numbers of observations. The estimation procedure was able to identify the parameters with different *nobs*, although the convergence rate was much slower with $nobs =$ 1. From these evolutions we see that even if $nobs =$ 1 is enough to recover the values of E and R_t, one should attempt to at least have 2 observations for faster convergence. The Young's modulus also appears to be simpler to identify than the reflection coefficient. This is possibly because the time required to propagate the information contained in any boundary condition throughout the whole domain is of order L/c, where L is the size of the network and c the wave speed. Instead, the Young's modulus directly impacts the wave speed so that it requires only Ls/c to feel any change in E, where $Ls < L$ is the distance between 2 consecutive observation locations. Table 7 shows the value of estimated Young's modulus and the reflection coefficients with errors (percentage deviation from target value) using different number of observations. In Figure 9C, the pressure solution obtained with the estimated parameters using $nobs =$ 2, at the first observation point on left carotid, is compared with the target and initial pressure profiles. The simulated and the target pressure waveforms have very similar shape with an error of less than 0.2% in the maximum pressure.

The next configuration involves a more realistic situation with available experimental data.

5.2 | A test case with experimental data

The efficiency of parameter estimation using the EnKF is presented, where experimental data are used as the observations. We refer to the experiment in Saito et al.,[24] where a simple human arterial network (see Figure 4) with 4 bifurcations was designed using polymer tubes ($E =$ 0.185 MPa) to validate the applicability of the blood flow model. The tubes are filled with water, and for realization of the reflection coefficients of approximately 0.5, silicone tubes are connected at the end of the tubes to act as virtual peripheral sites. A pulse flow with the profile of half a cycle of a sinusoidal wave is used as input from the pump. The period of the pulse is 0.3s with the total flow volume of 4.5 mL. The pressure waves propagating in the viscoelastic tubes were experimentally measured using a pressure sensor at 150mm from the second bifurcation, which in an actual human body roughly corresponds to the carotid artery of the neck.[24]

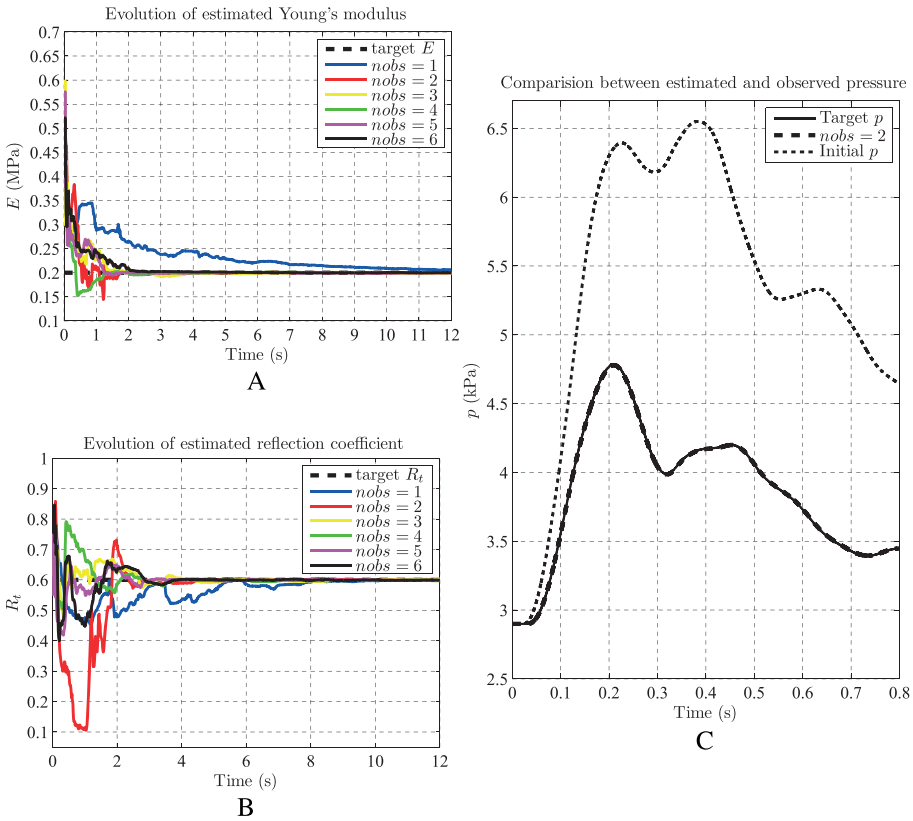

FIGURE 9 (A) The evolution of the Young's modulus using a different number of observations for case 2. The initial value is 0.4MPa and the target is 0.2MPa. (B) The evolution of the reflection coefficient using a different number of observations. The initial value is 0.8 and the target is 0.6. (C) The comparison between the pressure signal obtained with initially guessed parameters, the target pressure solution, and the one obtained by using the estimated parameters with $nobs = 2$, at $0.2L$ of the left carotid artery

TABLE 7 Test case 2: estimated Young's modulus and reflection coefficients with errors (percentage deviation from target values) using different numbers of observations

	Estimated E(MPa)	Estimated R_t	% deviation from target E	% deviation from target R_t
$nobs = 1$	0.2064	0.5995	3.20	− 0.08
$nobs = 2$	0.1993	0.6013	− 0.35	0.22
$nobs = 3$	0.1988	0.6030	− 0.60	0.50
$nobs = 4$	0.2006	0.5973	0.30	− 0.45
$nobs = 5$	0.1992	0.5994	− 0.40	− 0.10
$nobs = 6$	0.2003	0.5994	0.15	− 0.10

For this test case we do not know if the solution of the inverse problem exists, as the target has not been generated with the blood flow code. The aim is then to determine the best estimate of the Young's modulus (E), reflection coefficient (R_t), and viscoelastic coefficient (η) from the values of the experimentally measured pressure, which are taken as observations for the inverse problem. It is assumed that E and η are identical for all tubes and R_t is same at each terminal tube. The ensemble size $q = 20$ and the error covariance matrix $\mathbf{R}$ are defined as in Section 5.1.1. The pressure measurements are only available at 1 point on the carotid artery. The frequency of data assimilation is 0.01s.

To test the sensitivity to initial parameter values, we investigate the performance of the EnKF parameter estimation algorithm using 3 different sets of initial guess for the 3 parameters (E, R_t, and η). The mean values for the initial guess of the parameters were $(E\,(MPa), R_t, \eta\,(KPa{\cdot}s)) \in \{(0.2,\ 0.6,\ 0.3),\ (0.6,\ 0.3,\ 0.4)\}, (0.4,\ 0.8,\ 0.5)$. The estimated parameter values do not change significantly after 16s of EnKF assimilation as shown in Figure 10. From Figure 10, we see that the different guesses for initial mean values of the parameters seem not to have a significant impact on the converged assimilated result. The initial guess of the parameters and their best estimates obtained with their associated uncertainty (standard deviation) with three different initial guesses using the EnKF are shown in Table 8.

The blood flow model is then used with the estimated parameters to obtain the pressure profile at the observation

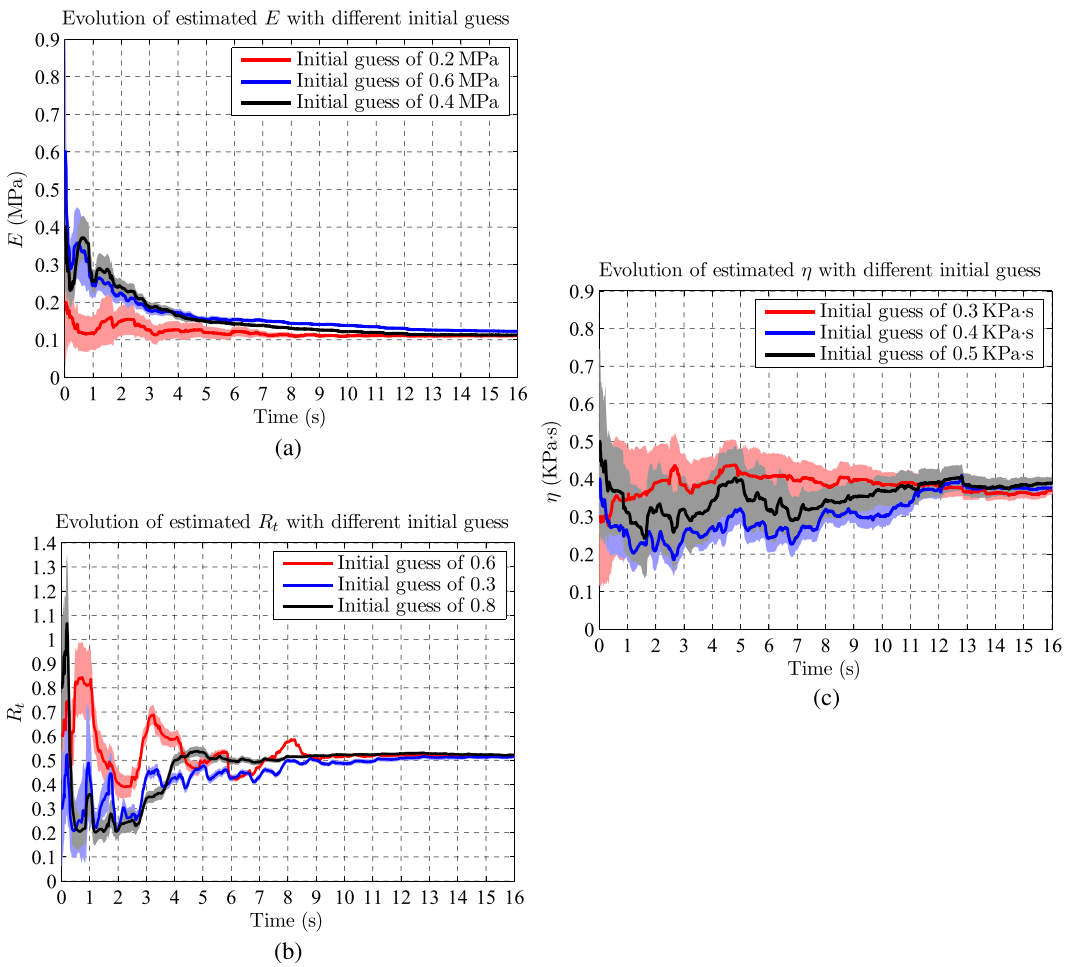

FIGURE 10 Sensitivity of ensemble Kalman filter parameter estimation to different sets of initial parameter values. (A)-(C), The evolution of Young's modulus, reflection coefficient, and viscoelastic coefficient respectively for the test case using the experimental data with different sets of initial values. The set of initial guess of the parameters, $\{E(MPa), R_t, \eta(kPa.s)\}$ are as follows: in red {0.2, 0.6, 0.3}, in blue {0.6, 0.3, 0.4}, and in black {0.4, 0.8, 0.5}. The shaded areas represent standard deviation around the mean values (solid lines)

TABLE 8 Sensitivity to initial parameter values for the test with experimental data. The initial guess of the parameters and their best EnKF estimates with their associated uncertainty (standard deviation)

Parameter	Initial guess	EnKF estimate	Error (± standard deviation)
E(MPa)	0.2	0.1111	0.0024
	0.6	0.1226	0.0025
	0.4	0.1150	0.0028
R_t	0.6	0.5199	0.0033
	0.3	0.5146	0.0075
	0.8	0.5290	0.0048
η(KPa·s)	0.3	0.3710	0.0124
	0.4	0.3760	0.0104
	0.5	0.3810	0.0157

Abbreviation: EnKF, ensemble Kalman filter.

point. Figure 11 shows the comparison between the pressure profile obtained with the 3 sets of estimated parameters, the numerical pressure profiles from the 1D blood flow model as reported in,[24] the measured pressure waves obtained from the experiment, and the pressure profile obtained from the 3 different sets of initial parameters. The simulated waveforms are similar to the target pressure waveform. We compare the systolic (maximum) pressure between the target (experimental pressure waveform) and the simulated pressures obtained from different sets of estimated parameters. The difference

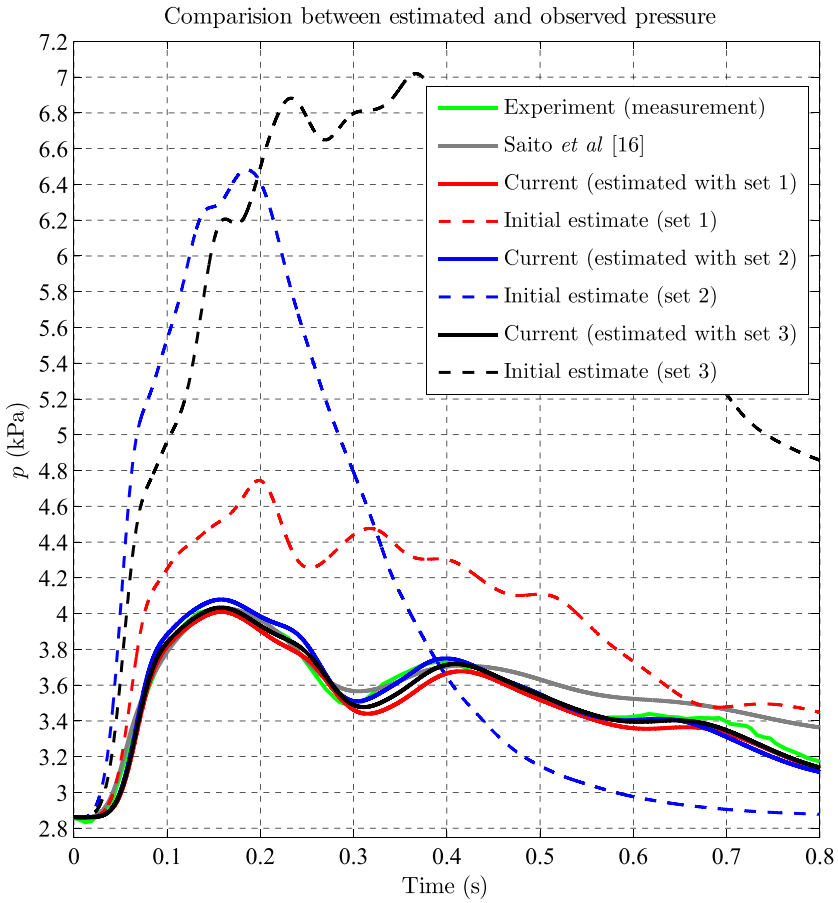

FIGURE 11 Comparison between the pressure profile obtained with the 3 sets of estimated parameters, the numerical pressure profiles from the 1D blood flow model as reported in Saito et al.,[24] the measured pressure waves obtained from the experiment, and the pressure profile obtained from the 3 different sets of initial parameters. The dashed lines are the initial pressure waveforms and the solid lines are the ones obtained from the estimated parameters. The set of initial guess of the parameters, $\{E(MPa), R_t, \eta(kPa.s)\}$, are as follows: set 1 {0.2, 0.6, 0.3}, set 2 {0.6, 0.3, 0.4}, and set 3 {0.4, 0.8, 0.5}

TABLE 9 Test case 3: comparison of the systolic (maximum) pressure between the target (experimental pressure waveform) and the simulated pressures obtained from different sets of estimated parameters

Estimated parameter set $\{E(MPa), R_t, \eta(kPa.s)\}$	Maximum pressure (MPa)	% error
set 1 (0.1111, 0.5199, 0.371)	4.01	− 0.24
set 2 (0.1226, 0.5146, 0.376)	4.08	1.50
set 3 (0.1150, 0.529, 0.381)	4.04	0.51

The target systolic pressure is 4.02 MPa.

is shown in Table 9. In all the cases the error is less than 2%. The results demonstrate that, even with $nobs = 1$, the Young's modulus, reflection coefficient, and the viscoelastic coefficient can be estimated with good accuracy using the proposed method.

6 | DISCUSSIONS

In this paper we have demonstrated the applicability of EnKF to estimate the Young's modulus, reflection coefficient, and viscoelastic coefficient. A similar approach can also be used to estimate other hemodynamics parameters such as resistance and compliance in a Windkessel model. The EnKF and thus the estimation algorithm provide the estimates of poorly known parameter values with their uncertainties. Sensitivity analysis with respect to the initial guess of parameters, the level of observation perturbation, the effect of bias in known parameter values, and the type of observations is carried out. Further analysis can be done on the efficiency of the estimation algorithm with respect to the locations of available observations. We need to make sure the size of the ensemble is correctly chosen. One also sees that very few spatial observation are necessary as the approach performs even with solely 1 spatial observation point. We also discussed the robustness of the inversion for different types of target observations (pressure or flow rate). We have shown a method of choosing an ensemble size using RMSE, but the efficiency of the EnKF parameter estimation algorithm may depend on other factors such as level of observation perturbation, the location of the observations, their types, and also the type of parameters to be estimated. The approach needs to be seen as a help to diagnosis tool and not a definite opinion. We mentioned that one issue is that uniqueness is not guaranteed. This might, therefore, impact clinical applications. Indeed, an incorrect Young's modulus might be obtained still providing a nice model fit, and obviously, this might mislead the clinician. The

approach, therefore, needs to be adopted in a Bayesian procedure with a priori information on the admissibility of the outcome by the clinicians and the outcome should definitely not been considered as a final opinion.

We aim at having an approach with moderate complexity to describe the physics of the problem and which is usable in practice. This is why any forward model based on a multi-dimensional flow model is out of the table. Other works, for instance, present data assimilation together with 3D flow models based on fully 3D Navier-Stokes,[18] which require heavy computational effort in addition to an increase in the complexity of the inverse problem. These approaches also require good know-how by the user and substantial learning efforts. We use a reduction in dimension to bring the cost of one state evaluation to the order of a minute on standard computers available in clinics. Then natural parallelism in EnKF makes a time to solution of the order of the number of EnKF iterations in minutes, which in the present case leads to approximately 2h. Still, this can be considered too costly and our current effort is to reduce complexity even further.

7 | STUDY LIMITATIONS

The first limitation of our current study is concerned with the size of the arterial network being adopted. We used a network consisting of 9 vessels, and the efficiency of the proposed estimation algorithm has to be tested for a larger arterial network, including complex network such as the circle of Willis in the cerebral vasculature. Second, an ensemble size of 20 is taken as an optimal size for the parameter estimation in the current study. An effect of taking a larger sample size on the estimation procedure can also be studied. The efficiency and convergence rate also depend on the level of observation perturbation, and another limitation is to identify the optimal level. It is also important to investigate the maximum number of parameters that can be estimated for a given arterial network with a given number of measurements available. In the current study we adopted 1D blood flow model with a constant resistance boundary condition. As discussed before, there is no real limitation regarding the boundary description, and thus, the estimation algorithm can be applied to a blood flow model coupled to a Windkessel model.

8 | CONCLUSION

A parameter estimation technique to compute the uncertain elastic and the terminal properties of networks of 1D blood vessels using the EnKF has been studied. The tests have been limited to the estimation of elastic moduli (Young's modulus) of the network, the reflection coefficient at the terminal vessels and the viscoelastic coefficient. The results confirm that the method is quite robust and permits to recover the arteries stiffness in a reasonable amount of time consistent with patient observation time at the hospital. Except with the computation of the Kalman gain, all the operations on the ensemble members are independent. This implies that their parallelization can be trivially carried out, thus decreasing the computational time needed to solve the inverse hemodynamics problem. The time to solution for this simulation is about 30min on a parallel computer with 20 cores, which is basically 1 node of the current standard distributions. The model simulations performed with the estimated parameter values produced accurate pressure profiles, which followed closely with the target profiles showing the effectiveness and the efficiency of both the estimation algorithm and the blood flow model. Also, it has been shown that the approach is effective with only a few observations, well suited to real clinical applications.

ACKNOWLEDGEMENTS

Research was done under the European Union Framework Programme Erasmus Mundus KITE (2013-2617 / 001-001 - EMA2).

REFERENCES

1. Benetos A, Waeber B, Izzo J, et al. Influence of age, risk factors, and cardiovascular and renal disease on arterial stiffness: clinical applications. *Am J Hypertens*. 2002;15(12):1101–1108.
2. Messas E, Pernot M, Couade M. Arterial wall elasticity: state of the art and future prospects. *Diagn Interv Imaging*. 2013;94(5):561–569.
3. Lorenc AC. Atmospheric data assimilation. Meteorological Office; 1995.
4. Lahoz W, Khattatov B, Menard R. *Data Assimilation: Making Sense of Observations*: Springer-Verlag Berlin Heidelberg; 2010.
5. Evensen G. The ensemble Kalman filter for combined state and parameter estimation. *IEEE Contr Syst*. 2009;29(3):83–104.
6. Annan J, Hargreaves J, Edwards N, Marsh R. Parameter estimation in an intermediate complexity earth system model using an ensemble Kalman filter. *Ocean Model*. 2005;8(1):135–154.
7. Anderson JL. An ensemble adjustment Kalman filter for data assimilation. *Mon Weather Rev*. 2001;129(12):2884–2903.
8. Gillijns S, De Moor B. Model error estimation in ensemble data assimilation. *Nonlinear Process Geophys*. 2007;14(1):59–71.
9. Baek SJ, Hunt BR, Kalnay E, Ott E, Szunyogh I. Local ensemble Kalman filtering in the presence of model bias. *Tellus A*. 2006;58(3):293–306.
10. Yang X, Delsole T. Using the ensemble Kalman filter to estimate multiplicative model parameters. *Tellus A*. 2009;61(5):601–609.
11. Liu J, West M. Combined parameter and state estimation in simulation-based filtering. *Sequential Monte Carlo Methods in Practice.* Springer New York; 2001:197–223.
12. Srikanthan R, Amirthanathan G, Kuczera G. Real-time flood forecasting using ensemble Kalman filter. *MODSIM 2007 International Congress on Modelling and Simulation. Modelling and Simulation Society of Australia and New Zealand*, Christchurch , New Zealand 2007:1789–1795.
13. Zupanski D, Zupanski M. Model error estimation employing an ensemble data assimilation approach. *Mon Weather Rev*. 2006;134(5): 1337–1354.
14. Godinez HC, Reisner JM, Fierro AO, Guimond SR, Kao J. Determining key model parameters of rapidly intensifying hurricane guillermo (1997) using the ensemble Kalman filter. 2011; arXiv preprint arXiv:1107.4407.
15. Massonnet F, Goosse H, Fichefet T, Counillon F. Calibration of sea ice dynamic parameters in an ocean-sea ice model using an ensemble Kalman filter. *J Geophys Res-Oceans*. 2014;119(7):4168–4184.

16. Lombardi D. Inverse problems in 1D hemodynamics on systemic networks: a sequential approach. *Int J Numer Method Biomed Eng*. 2014;30(2): 160–179.
17. Moireau P, Bertoglio C, Xiao N, et al. Sequential identification of boundary support parameters in a fluid-structure vascular model using patient image data. *Biomech Model Mechanobiol*. 2013;12(3):475–496.
18. Pant S, Fabrèges B, Gerbeau JF, Vignon-Clementel I. A methodological paradigm for patient-specific multi-scale CFD simulations: from clinical measurements to parameter estimates for individual analysis. *Int J Numer Method Biomed Eng*. 2014;30(12):1614–1648.
19. Bertoglio C, Moireau P, Gerbeau JF. Sequential parameter estimation for fluid-structure problems: application to hemodynamics. *Int J Numer Method Biomed Eng*. 2012;28(4):434–455.
20. Chabiniok R, Moireau P, Lesault PF, Rahmouni A, Deux JF, Chapelle D. Estimation of tissue contractility from cardiac cine-MRI using a biomechanical heart model. *Biomech Model Mechanobiol*. 2012;11(5):609–630.
21. Martin V, Clément F, Decoene A, Gerbeau JF. Parameter identification for a one-dimensional blood flow model. Proceedings, ESAIM, vol. 14. EDP Sciences. Centre International de Rencontres Mathematiques, Marseille, France, 2005:174–200.
22. Spilker RL, Taylor CA. Tuning multidomain hemodynamic simulations to match physiological measurements. *Ann Biomed Eng*. 2010;38(8):2635–2648.
23. Lassila T, Manzoni A, Quarteroni A, Rozza G. A reduced computational and geometrical framework for inverse problems in hemodynamics. *Int J Numer Method Biomed Eng*. 2013;29(7):741–776.
24. Saito M, Ikenaga Y, Matsukawa M, Watanabe Y, Asada T, Lagrée PY. One-dimensional model for propagation of a pressure wave in a model of the human arterial network: comparison of theoretical and experimental results. *J Biomech Eng*. 2011;133(12):121005.
25. Evensen G. Sequential data assimilation with a nonlinear quasi-geostrophic model using Monte Carlo methods to forecast error statistics. *J Geophys Res-Oceans (1978–2012)*. 1994;99(C5):10143–10162.
26. Thomas SJ, Hacker J, Anderson J. A robust formulation of the ensemble Kalman filter. *Q J R Meteorol Soc*. 2009;135(639):507–521.
27. Sakov P, Oke PR. A deterministic formulation of the ensemble Kalman filter: an alternative to ensemble square root filters. *Tellus A*. 2008;60(2): 361–371.
28. Evensen G. The ensemble Kalman filter: theoretical formulation and practical implementation. *Ocean Dynam*. 2003;53(4):343–367.
29. Houtekamer PL, Mitchell HL. Data assimilation using an ensemble Kalman filter technique. *Mon Weather Rev*. 1998;126(3):796–811.
30. Houtekamer P, Mitchell HL. Ensemble Kalman filtering. *Q J R Meteorol Soc*. 2005;131(613):3269–3289.
31. Hamill TM, Snyder C. A hybrid ensemble Kalman filter-3D variational analysis scheme. *Mon Weather Rev*. 2000;128(8):2905–2919.
32. Bishop CH, Etherton BJ, Majumdar SJ. Adaptive sampling with the ensemble transform Kalman filter. Part i: theoretical aspects. *Mon Weather Rev*. 2001;129(3):420–436.
33. Whitaker JS, Hamill TM. Ensemble data assimilation without perturbed observations. *Mon Weather Rev*. 2002;130(7):1913–1924.
34. Ott E, Hunt BR, Szunyogh I, et al. A local ensemble Kalman filter for atmospheric data assimilation. *Tellus A*. 2004;56(5):415–428.
35. Gillijns S, Mendoza OB, Chandrasekar J, De Moor B, Bernstein D, Ridley A. What is the ensemble Kalman filter and how well does it work? *Proceedings of the 2006 American Control Conference* Minneapolis, Minnesota, USA, June 14-16, 2006.
36. Shen Z, Tang Y. A modified ensemble Kalman particle filter for non-Gaussian systems with nonlinear measurement functions. *J Adv Model Earth Sy*. 2015.
37. Tang Y, Ambandan J, Chen D. Nonlinear measurement function in the ensemble Kalman filter. *Adv Atmos Sci*. 2014;31(3):551–558.
38. Mohammadi B. Ensemble Kalman filters and geometric characterization of sensitivity spaces for uncertainty quantification in optimization. *Comput Method Appl M*. 2015;290:228–249.
39. Burgers G, Jan van Leeuwen P, Evensen G. Analysis scheme in the ensemble Kalman filter. *Mon Weather Rev*. 1998;126(6):1719–1724.
40. Houtekamer PL, Mitchell HL. A sequential ensemble Kalman filter for atmospheric data assimilation. *Mon Weather Rev*. 2001;129(1): 123–137.
41. Ambadan JT, Tang Y. Sigma-point Kalman filter data assimilation methods for strongly nonlinear systems. *J Atmos Sci*. 2009;66(2):261–285.
42. Elsheikh AH, Pain C, Fang F, Gomes J, Navon I. Parameter estimation of subsurface flow models using iterative regularized ensemble Kalman filter. *Stoch Env Res Risk A*. 2013;27(4):877–897.
43. Sherwin S, Formaggia L, Peiro J, Franke V. Computational modelling of 1D blood flow with variable mechanical properties and its application to the simulation of wave propagation in the human arterial system. *Int J Numer Meth Fluids*. 2003;43(6-7):673–700.
44. Wang X, Fullana JM, Lagrée PY. Verification and comparison of four numerical schemes for a 1D viscoelastic blood flow model. *Comput Methods Biome*. 2015;18(15):1704–1725.
45. Peiró J, Veneziani A. Reduced models of the cardiovascular system. *Cardiovascular Mathematics*. Springer Milan; 2009:347–394.
46. Mynard J, Nithiarasu P. A 1D arterial blood flow model incorporating ventricular pressure, aortic valve and regional coronary flow using the locally conservative Galerkin (lcg) method. *Commun Numer Meth En*. 2008;24(5):367–417.
47. Blanco P, Watanabe S, Feijoo R. Identification of vascular territory resistances in one-dimensional hemodynamics simulations. *J Biomech*. 2012;45(12):2066–2073.
48. Quarteroni A, Formaggia L. Mathematical modelling and numerical simulation of the cardiovascular system. *Computational Models for the Human Body, Handbook of Numerical Analysis*, vol. 12. Elsevier, Amsterdam; 2004:3–127. doi: 10.1016/S1570-8659(03)12001-7.
49. Formaggia L, Lamponi D, Tuveri M, Veneziani A. Numerical modeling of 1d arterial networks coupled with a lumped parameters description of the heart. *Comput Methods Biome*. 2006;9(5):273–288.
50. Marchandise E, Willemet M, Lacroix V. A numerical hemodynamic tool for predictive vascular surgery. *Med Eng Phys*. 2009;31(1):131–144.
51. Formaggia L, Quarteroni A, Veneziani A. *Cardiovascular Mathematics: Modeling and Simulation of the Circulatory System*, vol. 1. Springer Milan; 2010.
52. Reymond P, Merenda F, Perren F, Rüfenacht D, Stergiopulos N. Validation of a one-dimensional model of the systemic arterial tree. *Am J Physiol-Heart C*. 2009;297(1):H208–H222.
53. Boileau E, Nithiarasu P, Blanco PJ, et al. A benchmark study of numerical schemes for one-dimensional arterial blood flow modelling. *Int J Numer Method Biomed Eng*. 2015;31(10): 1–33.
54. Formaggia L, Lamponi D, Quarteroni A. One-dimensional models for blood flow in arteries. *J Eng Math*. 2003;47(3-4):251–276.
55. Vignon IE, Taylor CA. Outflow boundary conditions for one-dimensional finite element modeling of blood flow and pressure waves in arteries. *Wave Motion*. 2004;39(4):361–374.
56. Du THD, Cai D. Outflow boundary conditions for blood flow in arterial trees. *PLoS ONE*. 2015;10(5):e0128597.
57. Alastruey J, Parker K, Peiró J, Sherwin S. Lumped parameter outflow models for 1-D blood flow simulations: effect on pulse waves and parameter estimation. *Commun Comput Phys*. 2008;4(2):317–336.

How to cite this article: Lal, R., Mohammadi, B., and Nicoud, F. (2016), Data assimilation for identification of cardiovascular network characteristics, *Int. J. Numer. Meth. Biomed. Engng.*, doi: 10.1002/cnm.2824